Supporting Information

Enhanced Permeability, Selectivity and Antifouling Ability of CNTs/Al_2O_3 Membrane under Electrochemical Assistance

Xinfei Fan, Huimin Zhao, Yanming Liu, Xie Quan, Hongtao Yu, and Shuo Chen*

Key Laboratory of Industrial Ecology and Environment Engineering (Ministry of Education, China), School of Environmental Science and Technology, Dalian University of Technology, Dalian 116024, China

*Corresponding author e-mail: quanxie@dlut.edu.cn

Number of pages: 18;

Number of Tables: 5;

Number of Figures: 16

1. Measurement of pore size distribution and porosity of CNTs/Al_2O_3 membrane

The liquid-liquid displacement porosimetry was used to investigate the pore size distribution according to Laplace's equation (1) and Hagen-Poiseuille equation (2).

$$\Delta P = \frac{2\sigma}{r} cos\theta \qquad (1)$$

$$Q = \frac{\pi}{8\tau l} \Delta P \int_{r_i}^{r_{max}} n r^4 dr \qquad (2)$$

where ΔP was the applied pressure, σ was the interfacial tension (1.7 mN/m for water/isobutanol), r was the equivalent pore radius, τ was the dynamic viscosity of the displacing fluid and l was the membrane thickness. A mixture of water/isobutanol (1/1, v/v) was chosen as the porosimetric solution in which the contact angle (θ) between the mixture and membrane was assumed as zero.

The porosity of CNTs/Al_2O_3 membrane was obtained from microscopic image analysis. This method has been widely used to characterize membrane parameters (such as porosity, pore density, mean pore radius and pore size distribution) and rejection performance.[1-3] Briefly, SEM images were first taken for microscopic observation of the membrane surfaces and cross-sections. The obtained images composed of 256 grey levels (magnification of 10,000×) were binarized at threshold level *T* of 135. This binarization process was performed on the public domain images processing and analysis software ImageJ (National Institutes of Health, USA). The porosity was calculated according to the following equation:

$$\varepsilon = \frac{A_P}{A_T} \times 100\% \qquad (3)$$

where ε is porosity, A_P is the total porous surface area and A_T is the total image membrane area.

2. Filtration setup and membrane module of cross-flow membrane system

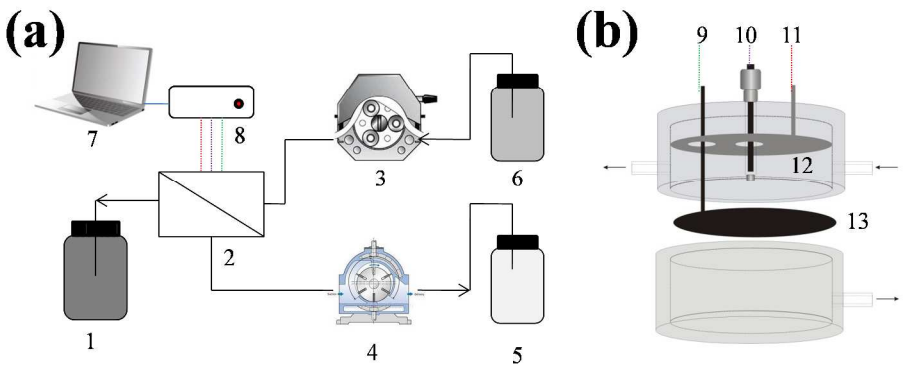

Figure S1. (a) Filtration setup and (b) membrane module of cross-flow membrane system. (1) concentrated water tank; (2) membrane module; (3) peristaltic pump; (4) vacuum pump; (5) effluent water tank; (6) feed water tank; (7) computer; (8) electrochemical system; (9) a perforated stainless steel column; (10) Ag/AgCl electrode; (11) a perforated Ti column; (12) Ti electrode; (13) CNTs/Al_2O_3 membrane.

Table S1 diameter and zeta potential of silica spheres and latex particles

Materials	**Diameter (nm)**	**zeta potential (mV)**
Silica spheres	140 ± 13	+ 7.6
Latex particles	57.7 ± 3.2	-8.4

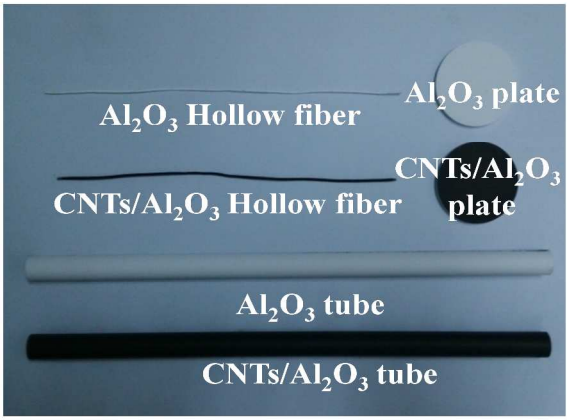

Figure S2. Al_2O_3 and CNTs/Al_2O_3 hollow fibrous, tabular and tubular membranes

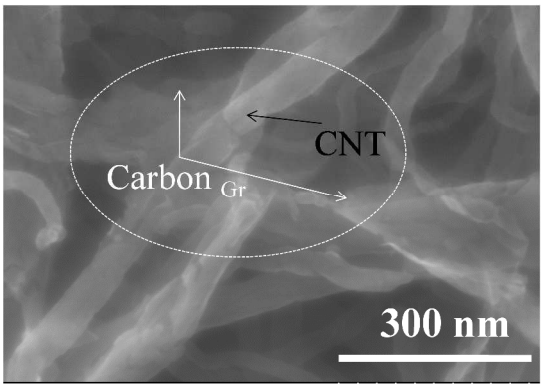

Figure S3. SEM image of graphene-like carbon at nodes between nanotubes.

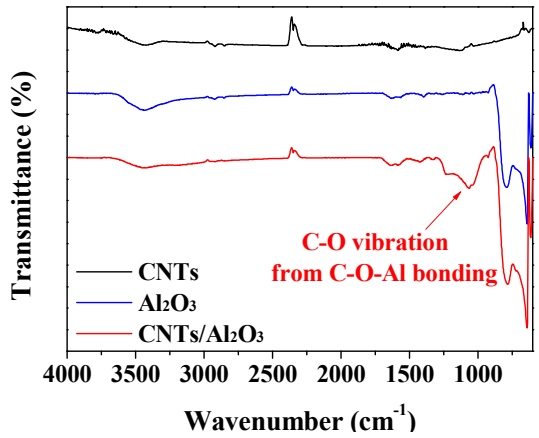

Figure S4. FT-IR analysis of CNTs, Al_2O_3 and CNTs/Al_2O_3

Table S2. Elastic strength, hardness, interfacial adhesion strength of membrane with/without graphene-like carbon (C_{Gr}).

Parameter	Membrane without C_{Gr}	Membrane with C_{Gr}
Elastic strength (GPa)	0.2±0.034	1.577±0.08
Hardness (MPa)	8±2	86±29
Critical interfacial stress (gf)	275	407

3. Ultrasonic and scouring tests of CNTs/Al_2O_3 membrane

In ultrasonic treatment of CNTs/Al_2O_3 membrane, only a slight CNTs loss of 3.5% was observed after 10 min ultrasonic treatment for the CNTs/Al_2O_3 membrane prepared with PAN (Figure S5). Negligible CNTs loss was found in further ultrasonic treatment for 20 min. In contrast, for CNTs membrane prepared by the same method but without PAN, significant CNTs loss of 86.7% occurred for 10 min ultrasonic treatment and the CNTs layer was completely damaged after being treated for further 20 min. It demonstrated that the graphene-like carbon can significantly strengthen the cross-linking points between the CNTs, leading to the good mechanical integrity of CNTs/Al_2O_3 membrane.

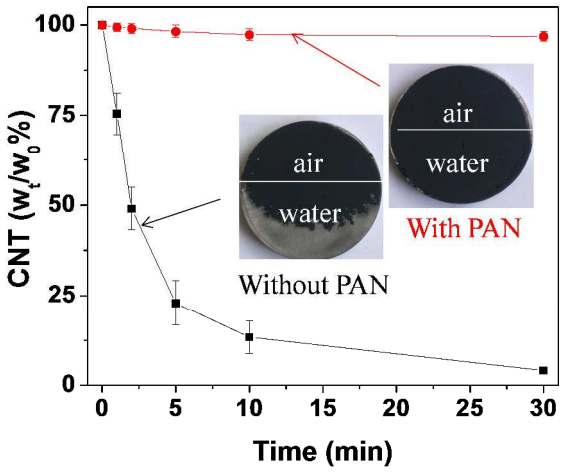

Figure S5. CNTs loss ratios of CNTs/Al_2O_3 membrane prepared with and without PAN in ultrasonic shock experiments. (Frequency: 40 kHz and power: 200 W).

To investigate CNT loss of CNTs/Al_2O_3 membrane during water treatment, the membrane was swept by cross flow for a long time of 600 min. The mass of CNTs loss was obtained by subtracting the mass of initial CNTs/Al_2O_3 membrane from that swept in ultrapure water for t min. (The mass of CNTs/Al_2O_3 membrane was measured by precision balance after dried at 100 °C in vacuum). As presented in Figure S6, slight CNTs loss did occur in the first 120 min (0.07%, 0.16%, 0.21% and 0.30% for shear rate of 0

m/s, 0.28 m/s, 0.54 m/s and 0.84 m/s, respectively), which might be resulted from washing away loosely attached CNTs in the membrane. While the CNTs mass loss was undetectable after 120 min, which indicated that CNTs did not be released anymore during water treatment. These results suggested the CNTs/Al_2O_3 membrane had good scouring resistance for long time operation.

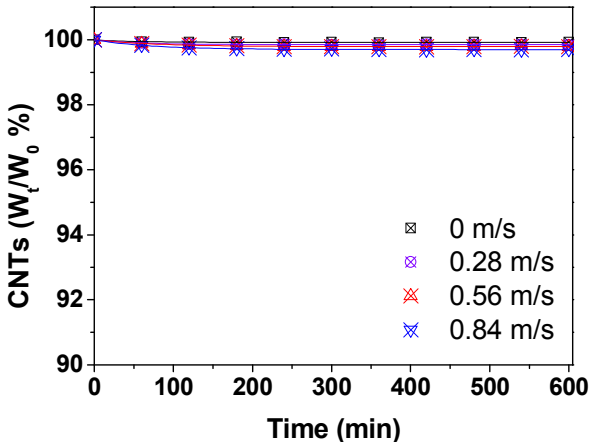

Figure S6. Effect of shear rate on CNTs loss (W_t: CNTs mass after swept for t min).

4. Adjustment of membrane pore size distribution and porosity

CNTs/Al_2O_3 membranes, with different CNTs area density (The mass of CNT loaded on per area of Al_2O_3 substrate), were characterized by analyzing their thickness, pore size distribution, porosity, electrical conductivity and permeability. As shown in the cross-section SEM images of CNTs/Al_2O_3 membranes (Figure S7a, S7c and S7e), thickness of CNTs layer increased proportionally with CNTs area density, which was 7, 12, or 20 μm as the CNTs area density was 0.5, 1.0, or 2.0 mg/cm^2, respectively. From the data of pore size distribution (Figure S7b, S7d and S7f)), it was also found the membrane pore size distributions depended on the CNTs area density. When the CNTs area density was 0.5 mg/cm^2, the pore size distributed from 108 to 234 nm with an average size of 171 nm. By increasing

the CNTs area density to 1.0 mg/cm^2, the pore size distribution became narrow, ranging from 109 to 176 nm, and the average pore size decreased to 142 nm. Further increasing CNTs area density to 2.0 mg/cm^2 resulted in much narrower pore size distribution (110~157 nm), where the average pore size decreased to 132 nm. In addition, the porosity of CNTs/Al_2O_3 membranes was 89.2%, 81.1%, or 73.2% for the CNTs area density of 0.5, 1.0, or 2.0 mg/cm^2, respectively (Table S3). These results suggested the thickness, pore size distribution, average pore size, and porosity can be adjusted by tuning CNTs area density on Al_2O_3 substrate. It was found both electroconductivity and pure water flux of the CNTs/Al_2O_3 membranes also depended on CNTs area density. The electroconductivity slightly increased from 1482.1 to 1657.4 S/m as CNTs area density increased from 0.5 to 2.0 mg/cm^2. These results illustrated CNTs/Al_2O_3 membrane had good electroconductivity and could work as a platform for combining membrane separation with electrochemistry. On the other hand, the pure water flux varied from 588 to 1370 L/m^2·h·bar with the CNTs area density decreasing from 2 to 0.5 mg/cm^2 (Figure S8).

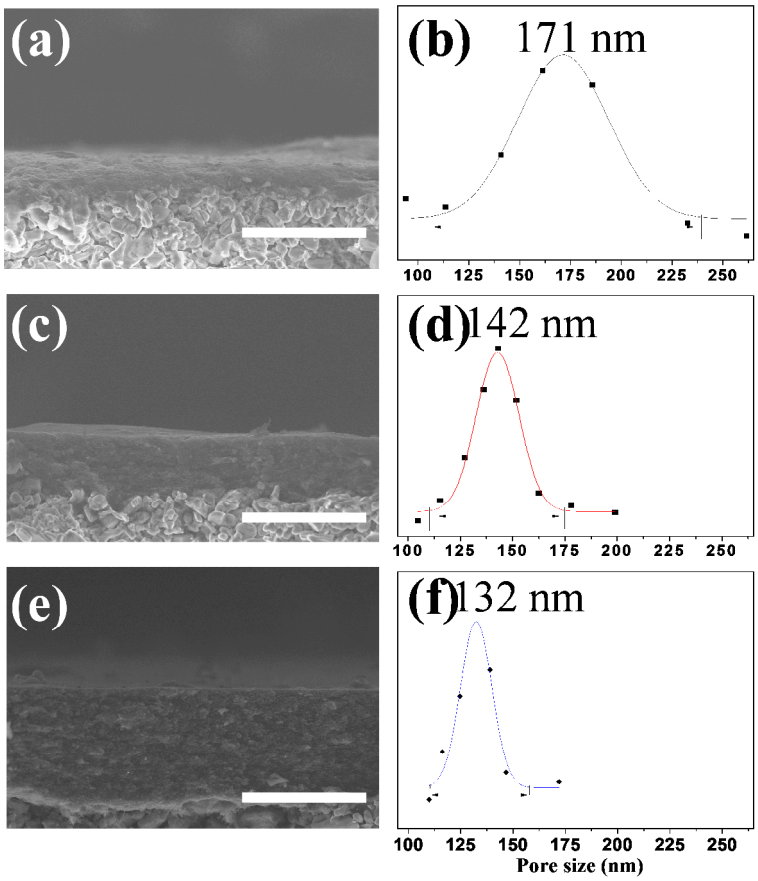

Figure S7. SEM cross-section images (bar: 20 μm) and pore size distributions of CNTs/Al_2O_3 membranes with CNTs area density of, (a) and (b) 0.5mg/cm^2; (c) and (d) 1.0 mg/cm^2; (e) and (f) 2.0 mg/cm^2.

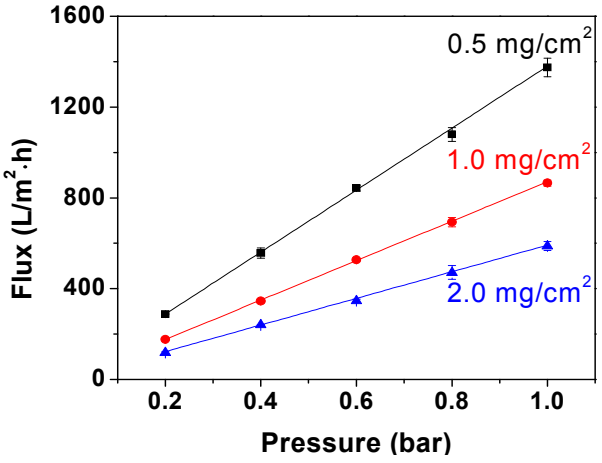

Figure S8. Pure water flux as a function of pressure for CNTs/Al_2O_3 membranes with CNTs mass area ratio of 0.5, 1.0, and 2.0 mg/cm^2.

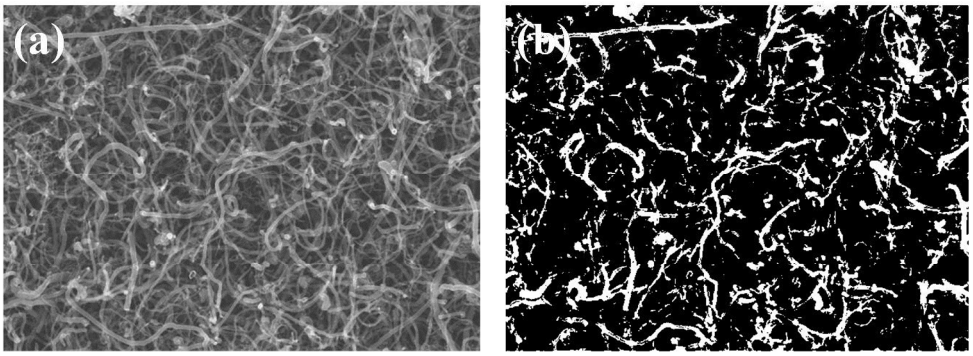

Figure S9. Microscopic images of CNTs/Al_2O_3 membrane at a magnification of 10,000 ×: (a) original image and (b) threshold image (at T= 135, porous surface was presented in black color).

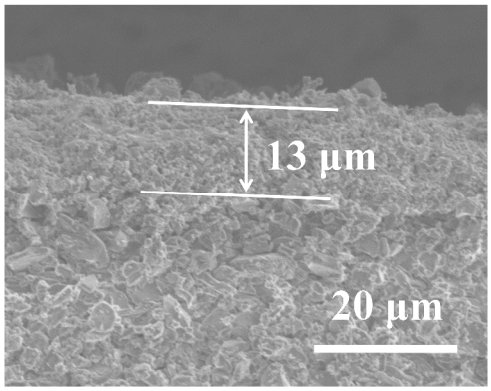

Figure S10. Cross section SEM image of ceramic membrane.

Table S3 porosity of CNTs/Al_2O_3 membranes with different CNTs mass area ratios

CNTs mass area ratio	Porosity (%)	Conductivity (S/m)
0.5	89.2	1482.1
1	81.1	1614.9
2	73.2	1657.4

Table S4 properties of pure Al_2O_3 membrane

Membrane	Pore size (nm)	Porosity (%)	Pure water flux ($L/m^2 \cdot h \cdot bar$)	Removal efficiency (Humic acid, %)
CM-150	150	37.1	593	8.9
CM-100	100	36.8	470	20

5. Electrochemical stability of CNTs/Al_2O_3 membrane

To investigate the electrochemical inertness of CNTs/Al_2O_3 membrane, electrochemical etching was performed at +1.5 ~ +2.0 V and then UV-vis absorption spectrum was used to characterize it because the adsorption spectrum of CNTs/Al_2O_3 membrane is related to the CNTs structure (such as diameter and length) to some extent. After treated at +1.5 V for 1 h, no obvious change is observed for the UV-vis adsorption of CNTs/Al_2O_3 membrane (Figure S11a). Besides, the individual CNT from the CNTs layer basically maintains their initial morphologies (inset of Figure S11a). These results suggest electrochemical etching of CNTs does not occur at +1.5 V. In contrast, after treated at +2.0 V for the same time, the UV-vis absorbance increases obviously and some CNTs have been broken (Figure S11b).

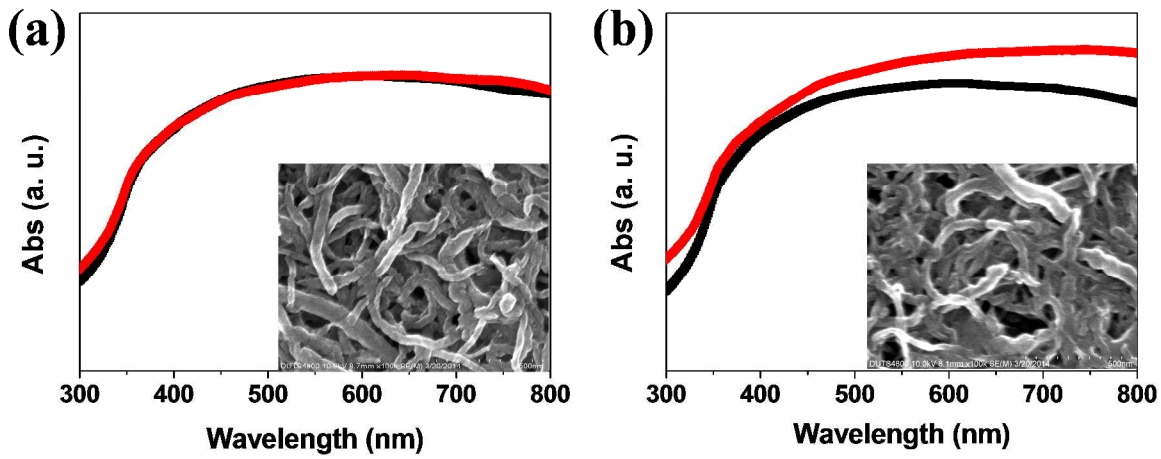

Figure S11. UV-vis spectrum of CNTs/Al_2O_3 membrane before (black curves) and after (red curves) electrochemical treated at (a) +1.5 V and (b) +2.0 V for 1 h (inert: SEM images of CNTs/Al_2O_3 membrane after electrochemical treatment), respectively.

Figure S12 shows the Raman spectrum of initial CNTs/Al_2O_3 membrane and the one after operating 600 min at +1.5 V. Both D peak (1332 cm^{-1}) and G peak (1580 cm^{-1}) can be observed. D peak is related to amorphous carbon or defects (sp^3 hybridization), while G peak is associated with graphitic carbon (sp^2 hybridization). Interestingly, the peak intensity ratio of D and G peak (I_D/I_G) had unobvious change after operating for 600 min at +1.5 V, suggesting negligible carbon oxidation occurred during filtration process.

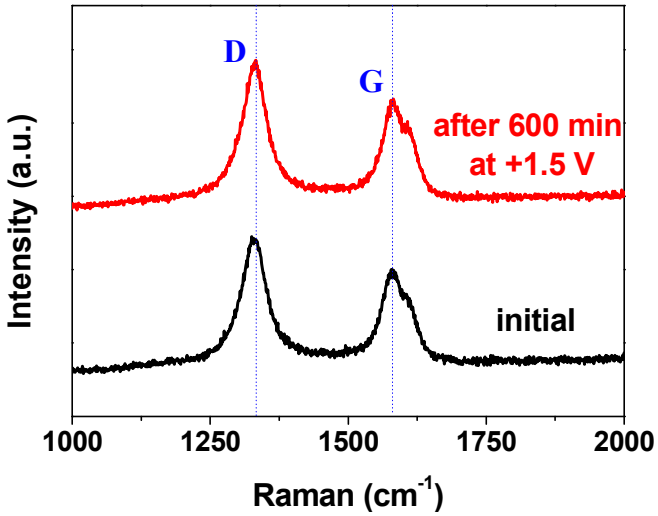

Figure S12. Raman spectrum of CNTs/Al_2O_3 before/after operating 600 min at +1.5 V.

6. Removal efficiency of silica sphere, latex particle, phenol and NOMs on porous substrate

As presented in Table S5, the removal efficiency on Al_2O_3 substrate after 30 min was 9.3% for silica spheres, 6.7% (log-reduction ratio) for latex particles, and 1.6% for humic acid, respectively. Meanwhile, no phenol can be rejected on Al_2O_3 substrate (phenol concentration in feed water and permeate water presented no discernable difference from HPLC). These results suggested almost all the pollutants used can pass through Al_2O_3 substrate, which was attributed to its low adsorption capability and much larger pore size relative to pollutant size. Since almost all the pollutants used can pass through Al_2O_3 substrate and Al_2O_3 substrate is nonconductive, it can be deduced that interaction of these pollutants with Al_2O_3 under electrochemical assistance was also negligible.

Table S5. Removal efficiency of silica spheres, latex particles and phenol on porous substrate (30 min).

Target	Removal efficiency
Silica spheres	9.3%
Latex particles	6.7% (log-reduction ratio)
Phenol	no
NOMs	1.6%

7. Effects of pH on silica sphere removal under electrochemical assistance

As presented in Figure S13, removal efficiency of silica spheres presented no obvious change when pH increased from 5 (99.1 %) to 7 (98.9 %). The same trend has been observed on normalized flux (98.2 % at pH5, 97.3% at pH7). However, when pH was 9, the removal efficiency of silica spheres declined to 91.1% and the normalized flux decreased to 79.2% of initial flux. Interestingly, only 3.3% and 5.7% of removed silica spheres were intercepted on the membrane surface at pH5 and pH7, while 19.5% of removed silica spheres was found on the membrane surface at pH9. To better understand these phenomena, zeta potential of silica spheres was measured, which were +19.1, +7.6 and -10.3 mV at pH of 5, 7 and 9, respectively. It can be found that the filtration performance declined dramatically as zeta potential of silica spheres changed from positive at pH7 to negative at pH9. At pH5 and pH7, electrostatic repulsion occurred between positively charged silica spheres and anodically polarized membrane, which was able to weaken the adhesion of silica spheres on membrane surface, resulting in the spheres swept away into cross-flow by shear force. The unobvious changed filtration performance when pH decreased from 7 to 5 might be due to that high removal efficiency and flux have already been

achieved at pH7. In contrast, electrostatic attraction occurred between negatively charged silica spheres and anodically polarized membrane at pH9, which might enhance the adhesion force between silica spheres and membrane, leading to an obvious flux loss and amount of silica spheres on membrane surface.

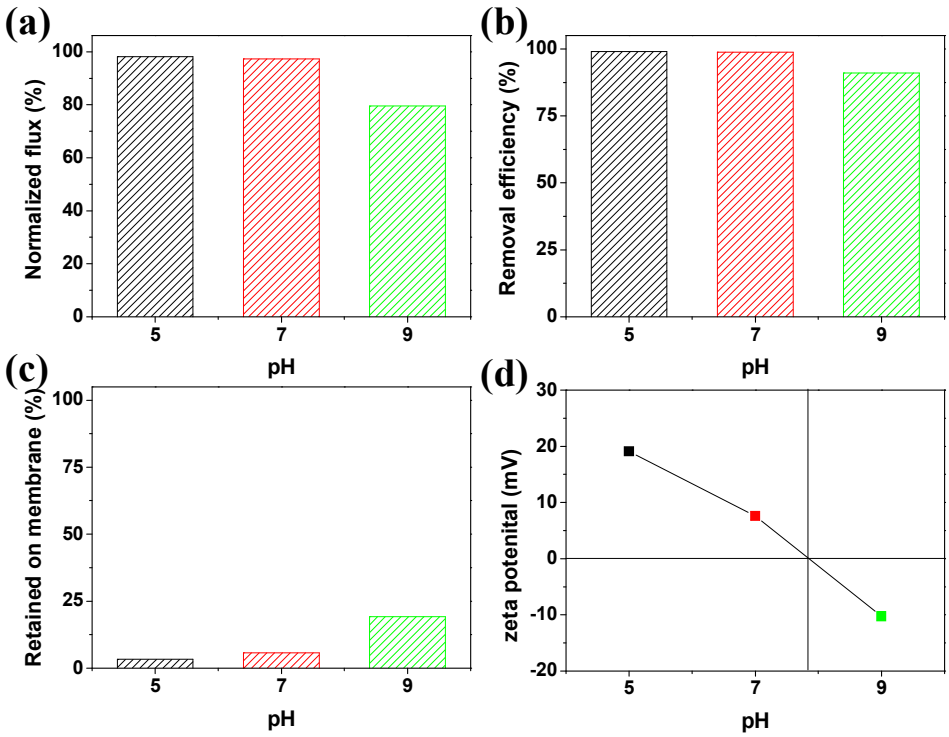

Figure S13. Effect of pH on filtration performance of CNTs/Al_2O_3 membrane for silica spheres removal at +1.5 V bias, (a) normalized flux, (b) removal efficiency, (c) retained ratio of silica spheres by size-exclusion and (d) zeta potential of silica spheres at pH of 5, 7 and 9.

8. Electrowetting of CNTs/Al_2O_3 membrane

It has been reported that electrochemistry can regulate the electrohydrodynamic behaviors of carbon materials, such as electrowetting and electrocapillarity.[1-4] Here, water contact angle of CNTs/Al_2O_3 membrane with/without electrochemical assistance were tested on an optical contact angle & interface

tension meter (SL200KB, Kino, USA). In brief, 10 mM Na_2SO_4 aqueous solution with constant volume (2 μL) was dropped on membrane surface and water contact angle was monitored over time. As seen in Figure S14, water contact angle declined as time increased either with or without bias applying, which was attributed to the dynamic behavior of the sessile drops of water on CNTs/Al_2O_3 membrane. Without bias applying, the plot of water contact angle versus time presented good linearity (R^2 = 0.996) with a slope (absolute value) of 0.08 °/ms, suggesting hydrophility of CNTs/Al_2O_3 membrane did not change without bias applying. However, the plot of water contact angle versus time presented nonlinear relationship (R^2 = 0.999) with a downward curvature at +1.5 V. The slope (absolute value) of its tangent line increased from 0.08 °/ms to 0.18 °/ms over time after applying bias, suggesting hydrophility of CNTs/Al_2O_3 membrane was improved by electrochemical assistance. The improved hydrophility was also contributed to the enhanced filtration performance of CNTs/Al_2O_3 membrane under electrochemical assistance.

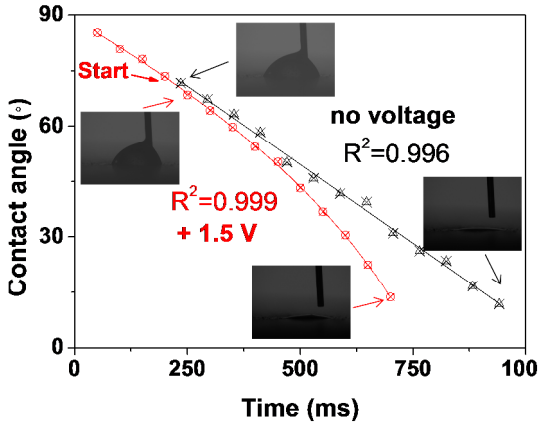

Figure S14. Water contact angle of CNTs/Al_2O_3 membrane with/without electrochemical assistance.

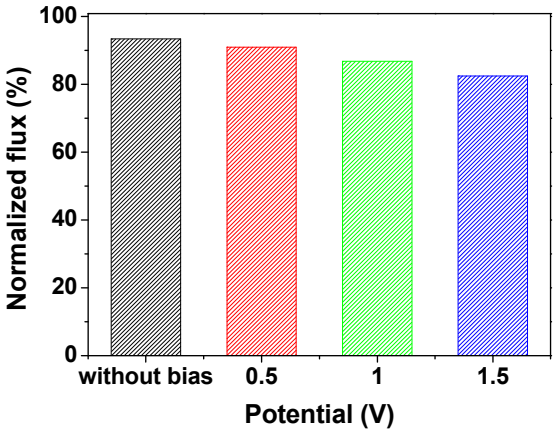

Figure S15. Flux of CNTs/Al_2O_3 membrane during latex particles removal at different bias.

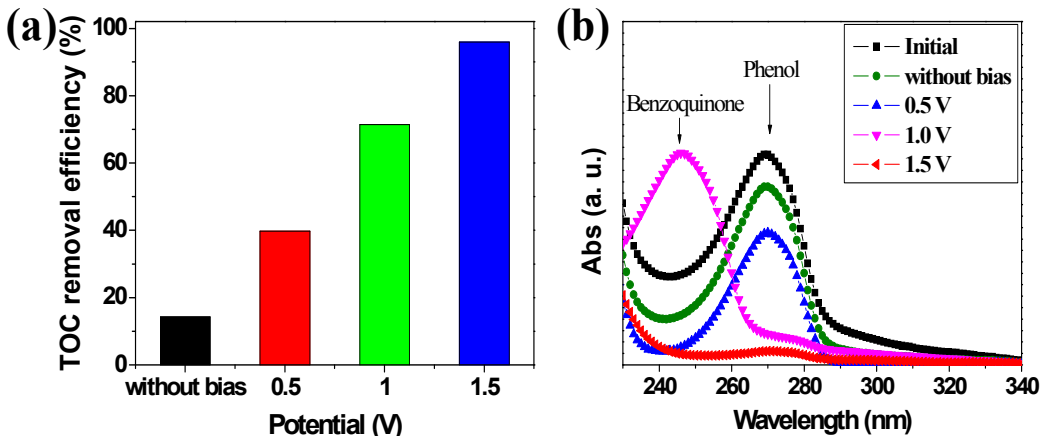

Figure S16. (a) TOC removal efficiency and (b) UV-vis spectrum of permeate water during phenol removal at different bias

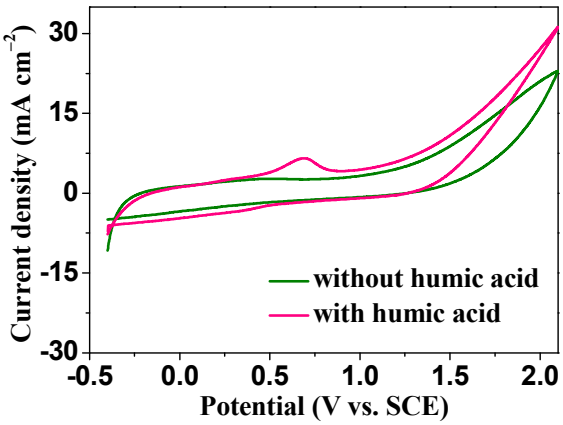

Figure S17. Cyclic voltammogram of CNTs/Al_2O_3 membrane in 0.1 M Na_2SO_4 with and without humic acid.

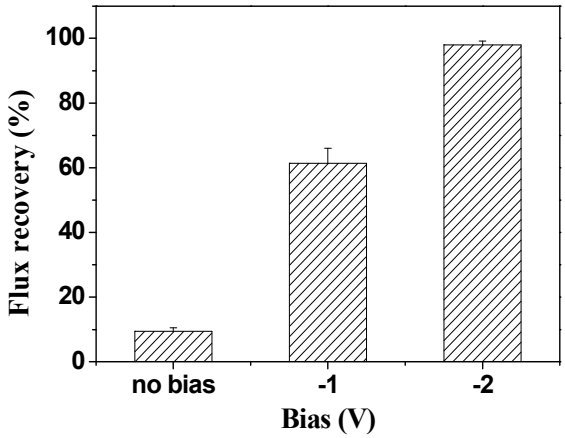

Figure S18. Flux recovery of CNTs/Al_2O_3 membrane by backwashing under different bias (membranes was fouled during NOMs removal under bias of +1.5 V for 1 h).

References:

(1) Masselin, I.; Durand-Bourlier, L.; Laine, J.-M.; Sizaret, P.-Y.; Chasseray, X.; Lemordant, D., Membrane characterization using microscopic image analysis. *J. Membr. Sci.* **2001,** *186*, (1), 85-96.

(2) Sun, W.; Chen, T.; Chen, C.; Li, J., A study on membrane morphology by digital image processing. *J. Membr. Sci.* **2007,** *305*, (1–2), 93-102.

(3) Wang, L.; Wang, X., Study of membrane morphology by microscopic image analysis and membrane structure parameter model. *J. Membr. Sci.* **2006,** *283*, (1–2), 109-115.

(4) Wang, Z.; Ci, L.; Chen, L.; Nayak, S.; Ajayan, P. M.; Koratkar, N., Polarity-dependent electrochemically controlled transport of water through carbon nanotube membranes. *Nano lett.* **2007,** *7*, (3), 697-702.

(5) Zhu, L.; Xu, J.; Xiu, Y.; Sun, Y.; Hess, D. W.; Wong, C.-P., Electrowetting of aligned carbon nanotube films. *J. Phys. Chem. B.* **2006,** *110*, (32), 15945-15950.

(6) Han, Z.; Tay, B.; Tan, C.; Shakerzadeh, M.; Ostrikov, K., Electrowetting Control of cassie-to-wenzel transitions in superhydrophobic carbon nanotube-based nanocomposites. *ACS Nano* **2009,** *3*, (10), 3031-3036.

(7) Pu, J. B.; Wan, S. H.; Lu, Z. B.; Zhang, G. A.; Wang, L. P.; Zhang, X. Q.; Xue, Q. J., Controlled water adhesion and electrowetting of conducting hydrophobic graphene/carbon nanotubes composite films on engineering materials. *J Mater Chem A* **2013,** *1*, (4), 1254-1260.